Ni single atoms anchored on N-doped carbon nanosheets as bifunctional electrocatalysts for Urea-assisted rechargeable Zn-air batteries

Hao Jiang [a], Jing Xia [b], Long Jiao [a], Xiangmin Meng [b], Pengfei Wang [b], Chun-Sing Lee [c], Wenjun Zhang [a,*]

[a] Department of Materials Science and Engineering, and Center of Super-Diamond and Advanced Films, City University of Hong Kong, 83 Tat Chee Avenue, Hong Kong Special Administrative Region
[b] Key Laboratory of Photochemical Conversion and Optoelectronic Materials, Technical Institute of Physics and Chemistry, Chinese Academy of Sciences, Beijing, PR China
[c] Department of Chemistry, and Center of Super-Diamond and Advanced Films, City University of Hong Kong, 83 Tat Chee Avenue, Hong Kong Special Administrative Region

ARTICLE INFO

ABSTRACT

The sluggish kinetics of oxygen electrode reactions is a bottleneck for the development of rechargeable Zn-air batteries (ZABs). Herein, we report a bifunctional electrocatalyst synthesized by anchoring individually dispersed Ni single atoms on N-doped carbon nanosheets (Ni SAs-NC), which exhibits an outstanding overall performance for oxygen reduction reaction (ORR) and urea oxidation reaction (UOR). Based on that, a conceptual urea-assisted rechargeable ZAB by coupling ORR with UOR of a low thermodynamic potential is demonstrated to have significantly decreased charging voltage and high urea elimination rate. The high bifunctional electrocatalytic activities of Ni SAs-NC endow the urea-assisted ZAB with a dramatically increased energy conversion efficiency of 71.8%, which is improved by 17.1% as compares with the conventional ZABs. The successful implementation of Ni SACs based urea-assisted rechargeable ZABs with an improved energy conversion efficiency may prompt ZAB technology towards practical applications.

1. Introduction

To cope with the growing energy demands and aggravating environmental problems, the exploration of renewable energy source and advanced energy storage devices has attracted broad research interests [1–4]. Rechargeable Zn-air batteries (ZABs) has a bright prospect for future grid-scale energy storage applications due to its low cost, environmental compatibility, outstanding safety, and high theoretical energy density (1084 Wh kg^{-1}) [5–7]. Nevertheless, critical challenges still remain in the development of ZABs owing to the sluggish kinetics and the poor reversibility of oxygen electrode reactions, i.e., oxygen reduction reaction (ORR) during discharging process and oxygen evolution reaction (OER) during charging process [8,9]. To this end, a variety of bifunctional oxygen electrode catalysts have been designed to boost the kinetics of ORR/OER and to reduce the voltage gap between the charging and discharging processes of ZABs, aiming to obtain a high overall energy efficiency [10–12]. Although remarkable progress has been made in the exploration of bifunctional oxygen electrode catalysts,

the performance of rechargeable ZABs is still not satisfactory, e.g., the energy conversion efficiency is generally below 60% [13–15]. Recent researches have demonstrated that the electrocatalytic oxidation reactions of some small molecule organics (urea, alcohols, glucose, 5-hydroxymethylfurfural, etc.) are more favorable than OER in alkaline electrolyte system [16,17]. Thus, to replace anodic OER (0.40 V vs. SHE) by the above oxidation reactions with more favorable kinetics and lower overpotentials will provide an opportunity to decrease the charging voltage and to improve the utilization efficiency for ZABs. Among them, urea oxidation reaction (UOR) could be an attractive substitution due to its low theoretical thermodynamic potential (−0.46 V vs. SHE), and vast and nearly cost-free source from urea-rich wastewater (such as urine) [17–19]. Additionally, electrochemical oxidation is also an effective method to treat urea-rich wastewater in industry. Therefore, the construction of urea-assisted rechargeable ZAB by coupling ORR and UOR can not only increase the overall energy conversion efficiency of ZAB, but also provide a potential solution to eliminate urea from the urea-rich wastewater.

* Corresponding author.
E-mail address: apwjzh@cityu.edu.hk (W. Zhang).

To ensure the high-efficiency operation of urea-assisted rechargeable ZABs, advanced ORR/UOR electrocatalysts with low overpotentials and high stabilities are required. For ORR, Pt-based noble metal is one of most canonized catalyst due to its high catalytic activity [20–22]. Nevertheless, the drawbacks of high cost and scarcity have limited their extensive applications. Thus, various non-noble metal electrocatalysts have been studied, and among them Ni-based electrocatalysts have aroused considerable interest owing to their promising ORR activity and low cost [23–25]. To further enhance their electrocatalytic performance toward ORR, a variety of morphologies and structures of these Ni-based catalysts have been elaborately designed to expose as much active sites as possible [26,27]. Recently, benefiting from the optimal atom utilization efficiency and highly exposed active sites, Ni single atom catalysts (SACs) have demonstrated their obvious superiority in achieving a high electrocatalytic activities for ORR [28–30]. For instance, Qiu et al. successfully prepared Ni single atoms/clusters supported on N-doped graphene (Ni-N-G), and revealed its remarkable performance as oxygen electrode catalysts in all-solid-state ZABs with an energy conversion efficiency of 60.9% [31]. On the other hand, the catalysts containing rich Ni sites, including Ni-based hydroxides, oxides, phosphides, nitrides and alloys, have also been verified to have notable UOR electrocatalytic activity [16,32,33]. Like those used in ORR, atomically dispersed Ni sites are also expected to endow preeminent electrocatalytic activity toward urea oxidation, but it has not been reported till now.

In this work, we report a facile synthesis of an electrocatalyst comprising Ni single atoms anchored on N-doped carbon nanosheets (Ni SAs-NC). Benefiting from the well dispersed and highly exposed Ni-N$_4$ sites, Ni SAs-NC has been demonstrated for the first time to have superior bifunctional electrocatalytic activity and outstanding stability towards both ORR and UOR in alkaline electrolyte. By using Ni SAs-NC as a bifunctional ORR/UOR catalyst in cathode, the constructed urea-assisted rechargeable ZABs is demonstrated to have a small charging/discharging voltage gap of 0.48 V, a high energy density of 831 Wh kg^{-1} and a long-term cycling life of 300 h. In particular, the battery is featured with an energy conversion efficiency of 71.8%, which is increased dramatically as compared with the conventional ZABs coupling ORR and OER under the same operation condition. Additionally, a urea elimination rate of 68.8 gm^{-2}h^{-1} is synchronously achieved at the cathode chamber with a charging current density of 100 mA cm^{-2}. The successful synthesis of Ni SACs bifunctional electrocatalysts towards ORR/UOR and the implementation of conceptual urea-assisted rechargeable ZABs will pave a new way for the development of practical electrochemical energy-storage devices with high energy conversion efficiency, and synergistic for the purification of urea-rich wastewater hopefully in the future.

2. Experimental section

2.1. Materials synthesis

2.1.1. Synthesis of Ni SAs-NC and Ni NPs-NC

Typically, 2.97 g Zn(NO$_3$)$_2$.6 H$_2$O and 10 mg Ni(NO$_3$)$_2$.6 H$_2$O were dissolved in 10 mL absolute ethanol solution, and 1.4 g hexamine (HMT) was dissolved in another 50 mL ethanol solution. After mixed the above two solutions under vigorous stirring, white ZnNi-hexamethylenetetramine (ZnNi-HMT) coordination framework precipitates were immediately produced. After centrifuging, washing and drying, ZnNi-HMT was pyrolyzed at 800 °C for 1 h with a heating rate of 5 °C min^{-1} under Ar protection. The obtained powders were etched with 3 M H$_2$SO$_4$ at 90 °C and rinsed with deionized water. After vacuum drying at 70 °C, the powders were pyrolyzed at 900 °C for 2 h to obtain Ni SAs-NC. As a reference sample, Ni nanoparticles anchored on N-doped carbon (Ni NPs-NC) was also synthesized by directly pyrolyzing ZnNi-HMT at 900 °C for 2 h. The other synthesis conditions were the same as those of Ni SAs-NC.

2.1.2. Synthesis of NC

To prepare nitrogen-doped carbon nanosheets (NC), the layered zinc-hexamethylenetetramine (Zn-HMT) coordination frameworks were first synthesized by the self-assembly of zinc nitrate hexahydrate and HMT in ethanol solution. The synthesis procedures of Zn-HMT were similar to those of ZnNi-HMT except for the absence of nickel nitrate hexahydrate in the precursor solution. After directly carbonizing the Zn-HMT at 900 °C for 2 h, the control sample of NC was obtained.

2.2. Materials characterization

X-ray diffraction (XRD, Philips X′ Pert) was employed to investigate the crystal structure of samples. The information of morphologies and elemental distribution of samples were acquired by scanning electron microscopy (SEM, Philips XL30 FEG) and the corresponding energy dispersive X-ray spectroscopy (EDS). The distribution and states of Ni atoms on the samples were characterized by a JEOL JEM-ARM300 F transmission electron microscopy (TEM)/scanning TEM (STEM) with a spherical aberration corrector (300 kV). X-ray photoelectron spectroscopy (XPS, VG ESCALAB 220i-XL) was carried out to reveal the chemical compositions of sample surfaces. Inductively coupled plasma optical emission spectrometer (ICP-OES, PerkinElmer 8300) was utilized to detect the metal content of samples. The microscopic pore structure of samples was analyzed by N$_2$ adsorption/desorption test (Quadrasorb SI, 77 K). X-ray absorption fine structure (XAS) spectra of samples at Ni K-edge were collected at the beamline 1W1B station of Beijing Synchrotron Radiation Facility (BSRF) to analyze the coordination environment of Ni sites. Ni foil, Ni Phthalocyanine (NiPc) and NiO were used as standard reference samples.

2.3. Electrochemical evaluation

Electrochemical measurements were performed on a CHI 760D electrochemical workstation linked with a rotating disk electrode (RDE, RRDE-3A, Japan) system. A glassy carbon electrode (Φ = 5 mm), Hg/HgO electrode and platinum foil (1 ×1 cm^2) were used as the working electrode, reference and counter electrodes, respectively. To evaluate the electrochemical performance of catalysts, a homogeneous catalyst ink (2 mg mL^{-1}) was prepared by dispersing catalyst powers in ethanol/Nafion solution (5 wt%, Sigma Aldrich) mixed solution. Then, catalyst ink was uniformly dropped onto the cleaned working electrode with a loading amount of 0.10 mg cm^{-2}. The reference electrocatalysts of Pt/C (20 wt%, Johnson Matthey) for ORR and RuO$_2$ (99.95 wt%, Sigma Aldrich) for UOR were prepared using the same methods with the identical areal mass loading. All the potentials were converted to reversible hydrogen electrode (RHE) by the formula of $E_{RHE} = E_{Hg/HgO}$ + 0.098 V + 0.059 ×pH.

2.3.1. ORR tests

The ORR performance of samples was evaluated by cyclic voltammetry (CV) and linear sweep voltammetry (LSV) measurements in 0.1 M KOH (5 mV s^{-1}). The kinetic current density (j_k) and transferred electron number (n) were calculated by Koutecky-Levich Eqs. (1–3):

$$\frac{1}{j} = \frac{1}{j_k} + \frac{1}{B\omega^{1/2}} \tag{1}$$

$$B = 0.2nFD_0^{2/3}\nu^{-1/6}C_0 \tag{2}$$

$$j_k = nFkC_0 \tag{3}$$

where j is the measured current density, ω is the electrode rotating speed, F is the Faraday constant (96485 C mol^{-1}), D_0 is the diffusion coefficient of O$_2$ (1.9 × 10^{-5} cm^2 s^{-1} for 0.1 M KOH), ν is the kinetic viscosity (0.01 cm^2 s^{-1}), and C_0 is the concentration of O$_2$ (1.2 × 10^{-6} mol cm^{-3}). The long-term stability of catalysts was evaluated by testing

the current-time (*i-t*) chronoamperometric responses at 0.6 V (vs. RHE) for 20 h.

2.3.2. UOR and OER tests

The UOR and OER performance of samples were evaluated by LSV measurements in 1.0 M KOH solution with or without 0.33 M urea. The bifunctional activity of catalysts is estimated by the potential difference (Δ*E*) between ORR and UOR:

$$\Delta E = {}^{UOR}E_{j10} - {}^{ORR}E_{1/2} \tag{4}$$

where $^{UOR}E_{j10}$ is the potential at a current density of 10 mA cm^{-2} for UOR, and $^{ORR}E_{1/2}$ is the half-wave potential for ORR.
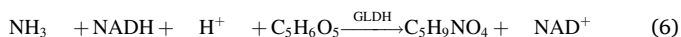
Electrochemical impedance spectroscopy (EIS) test was performed at 1.39 V (vs. RHE) with frequencies between 10 mHz and 100 KHz. The UOR stability of samples was tested by *i-t* responses at 1.39 V (vs. RHE) for 20 h in 1.0 M KOH+ 0.33 M urea solution. Electrochemical active surface areas (ECSA) were evaluated by measuring the double layer capacitance (C_{dl}) of samples.

2.4. Assembly and tests of urea-assisted rechargeable ZABs

To evaluate the overall performance of catalysts, the urea-assisted rechargeable ZABs were assembled by home-made electrochemical cells. Briefly, a pure Zn plate was used as anode with 4 M KOH+ 0.1 M Zn(Ac)$_2$ as anolyte. Ni SAs-NC loaded on the gas diffusion layer was used as air cathode with 4 M KOH+ 0.33 M urea as catholyte. The loading amount of Ni SAs-NC on air cathode was ~2.0 mg cm^{-2}. The anodic chamber and cathodic chamber were separated by a bipolar membrane (BMP) to prevent direct contact of the anolyte and catholyte. For comparison, conventional rechargeable ZABs were also assembled without BPM using 4 M KOH+ 0.1 M Zn(Ac)$_2$ as electrolyte. Polarization curve (*V-i*) was recorded by LSV technique on CHI 760D electrochemical workstation. Galvanostatic discharge/charge cycling (one cycle an hour) was performed in NEWARE (Shenzhen Neware Electronic Co. Ltd.) battery testing system. The electrolyte was refreshed every 30 h during the long-term discharge and charge cycling.

2.5. Measurement of urea elimination

Urease/glutamate dehydrogenase method was used to detect the amount of urea elimination [34]. The detection mechanism of urease/glutamate dehydrogenase method can be described as follows:

$$CH_4N_2O + H_2O \xrightarrow{Urease} 2NH_3 + CO_2 \tag{5}$$

$$NH_3 + NADH + H^+ + C_5H_6O_5 \xrightarrow{GLDH} C_5H_9NO_4 + NAD^+ \tag{6}$$

where NADH is nicotinamide adenine dinucleotide (reduced), $C_5H_6O_5$ is α-ketoglutaric acid, GLDH is glutamate dehydrogenase, $C_5H_9NO_4$ is glutamic acid, NAD$^+$ is nicotinamide adenine dinucleotide (oxidized). The decreased absorbance (Δ*A*) of NADH can be detected by spectrophotometer at 340 nm, which is proportional to the concentration of urea. The detection steps of urea by urease/glutamate dehydrogenase method were presented in the table below:

	Blank sample	Standard sample	Test sample
Deionized water (mL)	5	/	/
Standard solution (mL)	/	5	/
Test solution (mL)	/	/	5
Reagent 1^a (mL)	4	4	4
Shaking the mixed solution thoroughly and let it stand for 5 min			
Reagent 2^b (mL)	1	1	1
Shaking the mixed solution thoroughly and detecting the absorbance change (Δ*A*) of samples with 120 s intervals			

^{a} Reagent 1: tris buffer solution (100 mmol L^{-1}), α-ketoglutaric acid (15 mmol L^{-1}), glutamate dehydrogenase (1500 U L^{-1}). ^{b} Reagent 2: urease (800 U L^{-1}), nicotinamide adenine dinucleotide (reduced, 0.28 mmol L^{-1}).

The concentration of urea (C_{urea}) in test samples was calculated by Eq. (7):

$$C_{urea} = \frac{\Delta A_t - \Delta A_b}{\Delta A_s - \Delta A_b} \times C_s \tag{7}$$

where ΔA_t is the absorbance changes of test sample, ΔA_b is the absorbance changes of blank sample, ΔA_s is the absorbance changes of standard sample, C_s is the concentration of urea in standard sample (mmol L^{-1}).

The urea elimination rate of urea-assisted ZAB was calculated by Eq. (8):

$$\text{Urea elimination rate} = \frac{(C_0 - C_{urea}) \times V_{urea} \times M_{urea}}{S \times t} \tag{8}$$

where C_0 is the initial concentration of urea in electrolyte (0.33 mol L^{-1}), V_{urea} is the volume of electrolyte, M_{urea} is the relative molecular weight of urea (60.06 g mol^{-1}), S is the effective area of catalyst layer on cathode (cm^{-2}), t is the charging time of urea-assisted ZAB (h).

Faradaic efficiency (FE) of urea elimination through anodic UOR process was calculated by the equation of FE = (α × *m*×F)/Q, where α denotes the numbers of transferred electrons (α = 6 for UOR), *m* denotes the moles of gas products, and Q is the consumed charge.

3. Results and discussion

3.1. Working mechanism of urea-assisted rechargeable ZABs

Fig. 1a schematically illustrates the basic configuration and working mechanism of urea-assisted rechargeable ZAB, which mainly consists of a Zn electrode with KOH+Zn(Ac)$_2$ solution as anolyte, an air electrode with KOH+Urea solution as catholyte, and a bipolar membrane to allow ion transfer between two electrodes. During the discharging process, ORR occurs on the cathode driven by anodic Zn dissolution; and in the charging process, UOR takes place on the cathode, accompanied by Zn deposition on the anode. The specific reaction pathways and the associated calculations of the urea-assisted ZABs during discharging/charging processes are described in Eqs. S4-S9. In comparison with the OER process in conventional rechargeable ZABs (Eqs. S1), the charging cycle of urea-assisted ZABs is different and more readily to proceed due to the low thermodynamic potential of cathodic UOR. Theoretically, the constructed urea-assisted ZABs can be charged at a reduced voltage of 0.856 V (Fig. 1b), which is 0.794 V lowered than that of conventional rechargeable ZABs. Therefore, a high energy conversion efficiency is expected through replacing OER by UOR during the charging process of ZABs.

3.2. Synthesis and characterization of Ni SAs-NC

In this work, a composite comprising Ni single atoms anchored on N-doped carbon nanosheets (Ni SAs-NC) was prepared as ORR/UOR catalyst for urea-assisted rechargeable ZABs. The synthesis route of Ni SAs-NC is schematically illustrated in Fig. 2a. First, bimetal Zn/Ni-hexamine coordination frameworks (ZnNi-HMT) were prepared via a simple liquid phase deposition method as the precursor to synthesize Ni SAs-NC (Fig. S1). Like Zn-hexamine coordination frameworks (Zn-HMT), the as-prepared ZnNi-HMT have a 2D nanosheet morphology and a crystalline structure, as supported by the analyses of SEM, EDS and XRD in Fig. S2 to S4. ZnNi-HMT precursor was then pyrolyzed at 800 °C under Ar protection, followed by acid etching to remove metallic residues and a secondary pyrolysis at 900 °C to improve the graphitization degree of carbon matrix and to increase the content of Ni single atoms. The Zn nodes in the ZnNi-HMT precursor served as efficient space isolators to prevent the agglomeration of Ni atoms and promoted the generation of micropores on carbon nanosheets during the high-
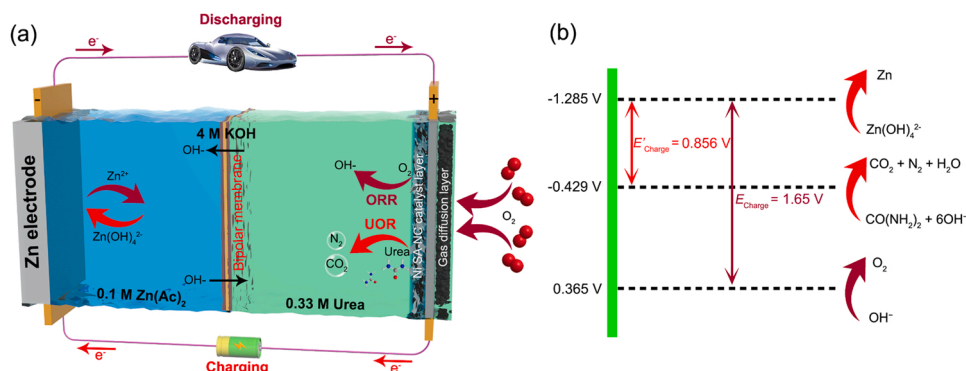
Fig. 1. Schematic illustration of charging/discharging processes for urea-assisted rechargeable ZABs. (a) The basic configuration and working mechanism of urea-assisted ZABs. (b) Comparison of the theoretical charging voltages of urea-assisted and conventional ZABs.

temperature pyrolysis [35]. Notably, the volatile Zn species with low boiling points were ultimately removed after the acid etching and high-temperature pyrolysis (up to 900 °C). As a result, Ni SAs-NC was obtained. In addition, to comparatively study the effects of Ni sites and the degree of their exposure on the electrocatalytic activity, nitrogen-doped porous carbon nanosheets (NC) and nitrogen-doped carbon nanosheets anchored with Ni nanoparticles (Ni NPs-NC) were also prepared. The SEM images of NC and Ni NPs-NC are presented in Fig. S5 and S6, respectively.

The SEM images in Fig. 2b-d show that Ni SAs-NC has a crumpled and interconnected nanosheet morphology; and no Ni nanoparticle is observed in the enlarged views by scanning transmission electron microscopy (STEM) (Fig. 2e). Moreover, as presented in the aberration-corrected HAADF-STEM images in Fig. 2f and g, monodispersed atomic-scale Ni species are observed on the nanosheets, corresponding to the isolated Ni single atoms. The EDS analysis verifies the existence of C, N, Ni and O elements in Ni SAs-NC (Fig. S7); and the STEM and corresponding EDS mapping images in Fig. 2h to l further reveal the uniform distribution of above elements in Ni SAs-NC. The content of Ni in Ni SAs-NC is detected to be 1.57 wt% by ICP-OES (Table S2).

XRD patterns in Fig. 3a display a broad diffraction peak at ~24.5° for all of NC, Ni NPs-NC and Ni SAs-NC samples, belonging to the (002) plane of graphitic carbon [30,36]. In addition, three weak diffractions at 44.5°, 51.8° and 76.1° are detected for the Ni NPs-NC, corresponding to the (111), (200), and (220) planes of metallic Ni, respectively (JCPDS No. 04–0850) [37]. The absence of metallic Ni peaks in the XRD pattern of Ni SAs-NC indirectly confirms that Ni species in Ni SAs-NC are highly dispersed at the atomic scales, which coincides well with the results of HAADF-STEM observations. Raman spectra show that the I_D to I_G ratio (I_D/I_G) of Ni SAs-NC (0.94) is slightly higher than those of NC (0.88) and Ni NPs-NC (0.89), indicating the existence of more structural defects in Ni SAs-NC (Fig. S8) [7,31]. In addition, the N_2 adsorption/desorption curves of above samples display typical type-IV isotherms with hysteresis loops, suggesting their mesoporous structures (Fig. S9) [35]. Nevertheless, owing to the removal of metal residues during acid etching and the evaporation of Zn in the pyrolysis process, the Ni SAs-NC affords a higher specific surface area (481 m^2 g^{-1}) and a larger pore volume (0.514 cm^3 g^{-1}) than those of Ni NPs-NC and NC (Table S1), which are beneficial to enhance their accessibility to the reactant, and thus accelerate the ion/mass transfer during electrocatalytic reactions [38].

XPS test was carried out to study the chemical compositions of these catalysts. As shown in Fig. S10 and Table S2, C, N, Ni and O are revealed on both Ni SAs-NC and Ni NPs-NC, while only C, N and O signals are detected on NC. In the core-level Ni 2p spectra of Ni NPs-NC (Fig. 3b), two peaks at 853.2 and 870.6 eV are ascribed to metallic Ni^0, and the peaks at 855.4 and 872.7 eV correspond to oxidized Ni^{2+} [39]. Unlike the Ni NPs-NC, the binding energy of Ni 2p$_{3/2}$ (854.7 eV) and Ni 2p$_{1/2}$ (871.8 eV) in Ni SAs-NC are between those of Ni^0 and Ni^{2+}, suggesting the Ni atoms in Ni SAs-NC situate in a low-valent oxidation state due to

the possible Ni-N coordination [40,41]. As regards the C 1 s XPS spectra (Fig. S11a), the triple sub-peaks at ~284.6, ~286.2 and ~287.9 eV are ascribed to C-C, C-N and C-O bonding, respectively [31,35]. The N 1 s spectrum can be decomposed into four nitrogen configurations, including pyridinic N (398.4 eV), pyrrolic N (399.6 eV), graphitic N (400.8 eV) and oxidized N (402.5 eV), respectively (Fig. S11b and Table S3) [30,42]. Owing to its favorable hybridization capability with the d orbitals of transition metal atoms, the pyridinic-N is generally identified as the coordinating site to trap and anchor metal atoms [41, 43].

The coordination environment and local electronic structure of atomic-scale Ni sites in Ni SAs-NC were explored by XAS. Fig. 3c displays the normalized X-ray absorption near-edge structure (XANES) spectrum of Ni SAs-NC at the Ni K-edge, with Ni foil, Ni Phthalocyanine (NiPc) and NiO as references. The adsorption edge of Ni SAs-NC sits between those of NiO and Ni foil, demonstrating the average valence of Ni single atoms in catalyst is between zero-valent Ni^0 and oxidized Ni^{2+}, which is agreeing with the XPS results. In addition, the XANES spectrum of Ni SAs-NC has characteristic peaks similar to those of NiPc, where the peaks of A (pre-edge at ~8332 eV), B (pre-edge at ~8338 eV), C (absorption edge at ~8350 eV) and D (post-edge at ~8356 eV) are attributed to the 1 s→3d transition, 1 s→4p$_z$ transition, 1 s→4p$_{x,y}$ continuum states and multiple scatter processes, respectively. Among them, the 1 s→4p$_z$ electronic transition of Ni cations is generally identified as the finger print of square-planar Ni-N$_4$ moiety [44–46]. Whereas, the XANES spectrum of Ni NPs-NC is remarkably similar to that of Ni foil due to the weak Ni-N interaction (Fig. S12). Based on the k^3-weighted Fourier transform (FT) of the extended X-ray absorption fine structure (EXAFS) at Ni K-edge, the local structural information around Ni sites can be further verified. As presented in Fig. S12, the Ni NPs-NC displays a prominent coordination peak at ~2.18 Å, which is attributed to the dominant Ni-Ni bonding. Unlike Ni NPs-NC, the Ni SAs-NC presents a dominant first shell peak at ~1.40 Å (Fig. 3d), corresponding to the Ni-N bonding in Ni-N$_x$ moieties [40,46]. The position of Ni-N peak is close to that of well-defined Ni-N$_4$ bonding in NiPc (~1.47 Å) and lower than those of Ni-Ni bonding (~2.18 Å) in Ni foil and Ni-O bonding (~1.6 Å) in NiO, indicating that the Ni single atoms in Ni SAs-NC are primarily bonded with N [40,47]. The fitting results of EXAFS curve show the coordination number of Ni and N atoms in Ni SAs-NC is close to 4, implying the formation of approximate Ni-N$_4$ coordination structure. (Fig. S13). From the above analysis, it can be concluded that Ni species in Ni SAs-NC exist dominantly as single atoms coordinated with N.

3.3. Electrocatalytic ORR performance of Ni SAs-NC

The ORR activity of catalysts was primarily evaluated by CV and LSV measurements in 0.1 M KOH. As presented in Fig. 4a, the CV response with the introduction of O$_2$ displays a distinct reduction peak at 0.86 V (vs. RHE) for Ni SAs-NC, and the peak position is close to that of
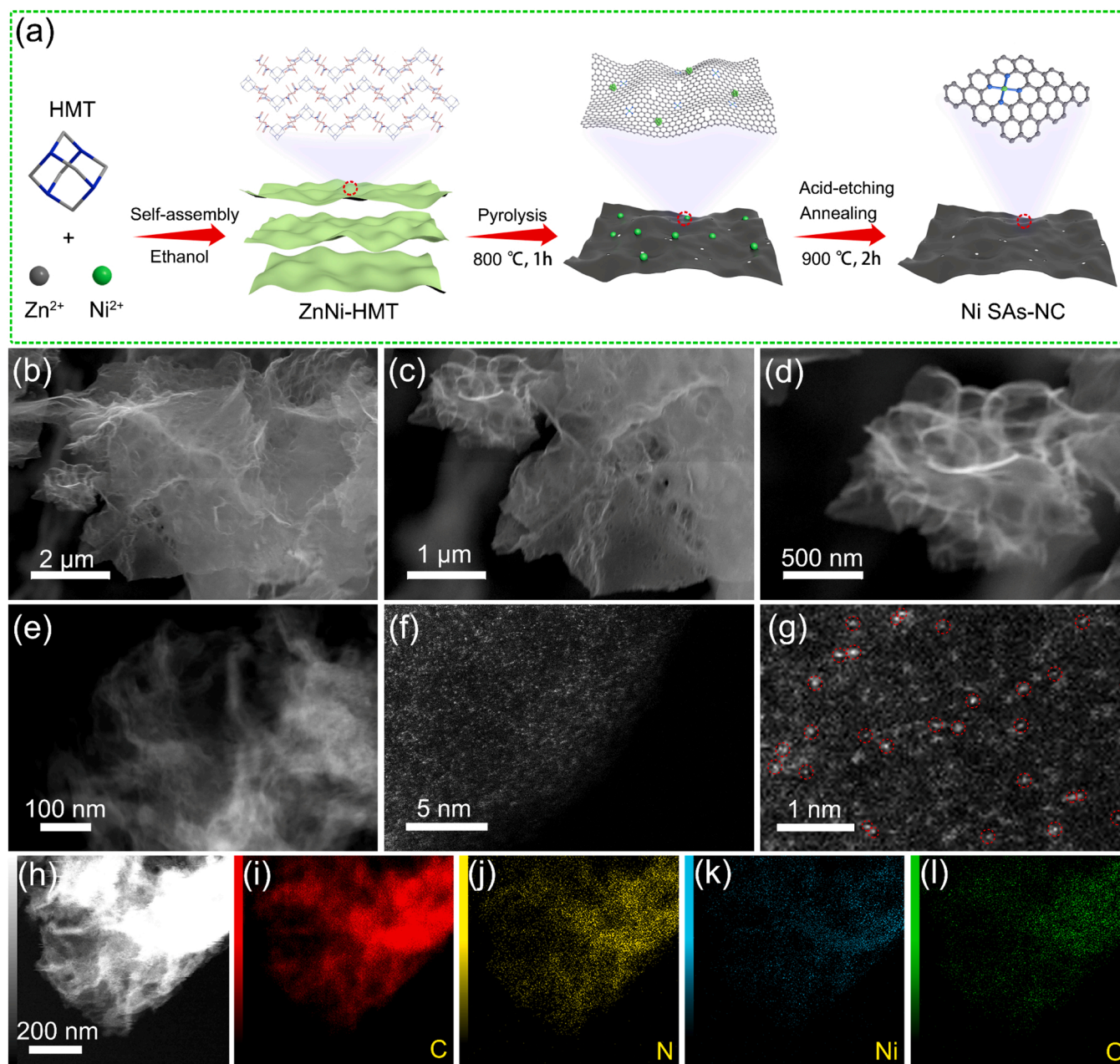
Fig. 2. (a) Schematic illustration of the preparation process of Ni SAs-NC. (b-d) SEM images of Ni SAs-NC with different magnifications. (e) STEM and (f, g) aberration corrected HAADF-STEM images of Ni SAs-NC. A fraction of atomic-scale Ni species is highlighted representatively in (g). (h) Dark field STEM and (i-l) the corresponding EDS mapping images of Ni SAs-NC.

commercial Pt/C (Table S4), which suggest a high ORR activity of Ni SAs-NC. The LSV curves in Fig. 4b show that Ni SAs-NC holds a half-wave potential ($^{ORR}E_{1/2}$) of 0.85 V, which is equal to that of Pt/C and much positive than those of Ni NPs-NC (0.80 V) and NC (0.71 V). Moreover, the ORR activity of Ni SAs-NC is also comparable to those of prominent non-noble metal SACs, e.g., Fe-SA-NSFC (0. 91 V) [48], CoSA/N,S-HCS (0.85 V) [49], N-Mo-G (0.85 V) [50], MnNC-900 (0.82 V) [51], and as well some more examples as summarized in Table S5. The superior ORR activity of Ni SAs-NC is further verified by its large j_k value (4.75 mA cm^{-2}) at 0.8 V (Fig. 4c), which is higher than those of Pt/C (4.72 mA cm^{-2}), Ni NPs-NC (0.90 mA cm^{-2}) and NC (0.15 mA cm^{-2}). By normalizing the current density with respect to the metal content based on ICP results, the mass activity of these catalysts is calculated and displayed in Fig. 4d. Remarkably, Ni SAs-NC has a high mass activity of 1.57 A mg$_{Co}^{-1}$ at 0.85 V, which is approximately 7 times

and 12 times higher than those of Ni NPs-NC (0.22 A mg$_{Co}^{-1}$) and Pt/C (0.13 A mg$_{Pt}^{-1}$), respectively, revealing the high utilization of Ni activity sites at atomic scale.

Tafel slope is a key metrics to estimate the reaction kinetics of catalysts. As displayed in Fig. 4e, the Tafel slope of Ni SAs-NC (56 mV dec^{-1}) only slightly overtops that of Pt/C (54 mV dec^{-1}) but much lower than those of other reference catalysts, suggesting its favorable ORR kinetics [52]. The ORR kinetics and reaction pathway of these catalysts were further investigated by RDE measurements at 400–1600 rpm. As shown in Fig. S14, the limit diffusion current of catalysts increases linearly with the rotation speed. The nearly parallel Koutecky-Levich (K-L) plots reveal a first-order reaction kinetics for the dissolved O$_2$ (Fig. S15) [52,53]. The average electron transfer number (n) of metal-free NC is calculated to be 3.23 based on the K-L equation (Fig. S15a), pointing towards a mixed ORR pathway. In contrast, the n for Ni SAs-NC is
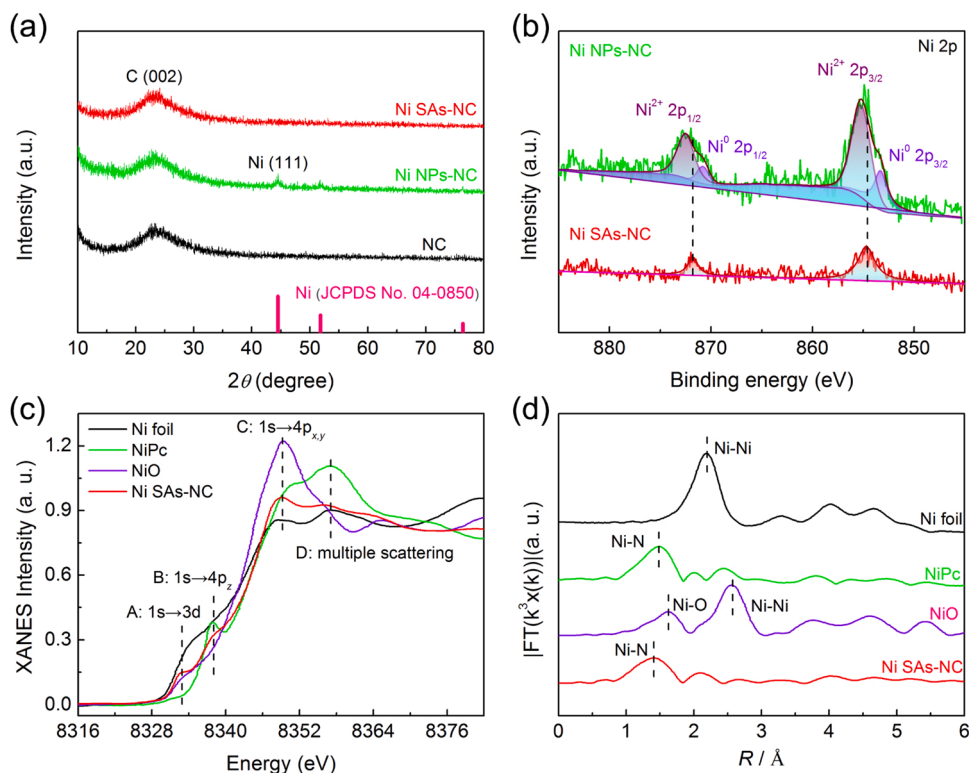
Fig. 3. (a) XRD patterns of NC, Ni NPs-NC and Ni SAs-NC. (b) Ni 2p XPS spectra of Ni NPs-NC and Ni SAs-NC. (c) Ni K-edge XANES spectra of Ni SAs-NC and reference samples, Ni foil, NiPc, and NiO. (d) FT-EXAFS curves of Ni SAs-NC and reference samples at Ni K-edge.
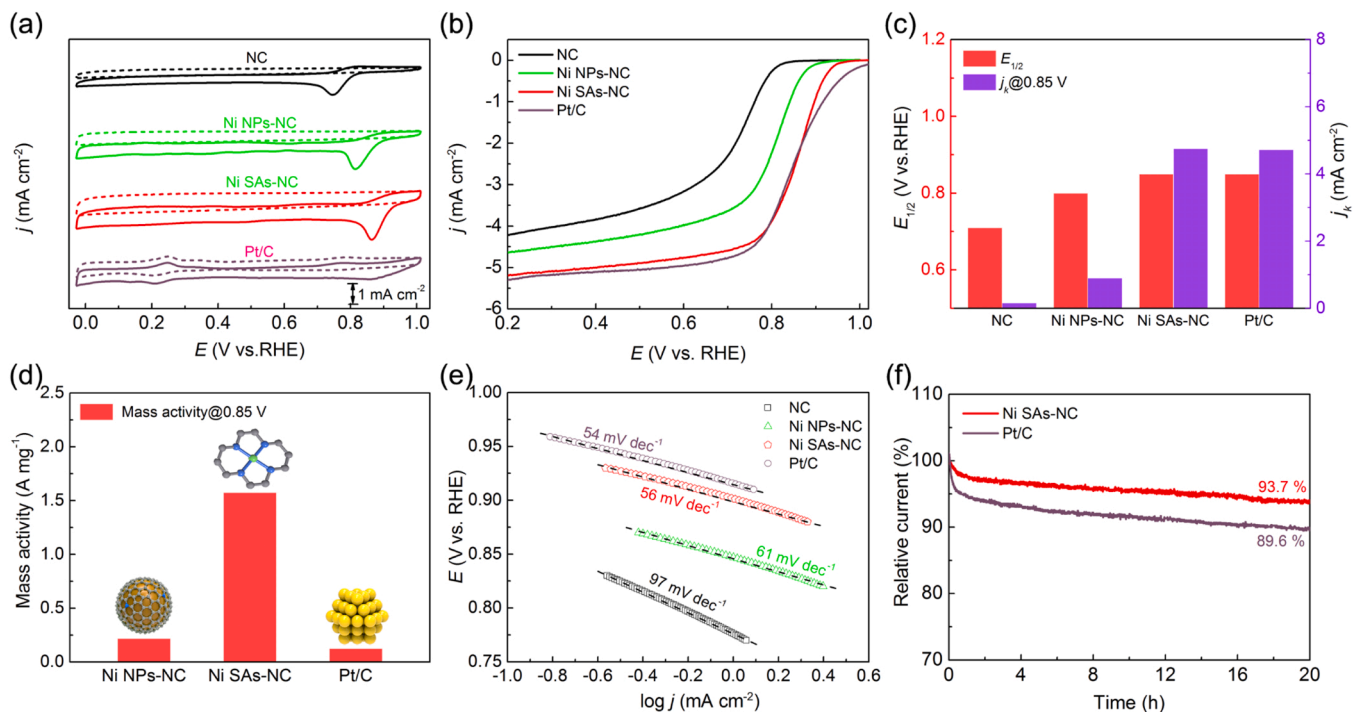

Fig. 4. (a) CV curves of different catalysts in O_2/N_2 saturated 0.1 M KOH. (b) LSV curves of different catalysts in O_2 saturated 0.1 M KOH. (c) Comparison of $^{ORR}E_{1/2}$ and j_k for different catalysts. (d) Tafel plots of different catalysts. (e) Comparison of mass activity of Ni NPs-NC, Ni SAs-NC and Pt/C at 0.85 V. (f) Chronoamperometric response of Ni SAs-NC and Pt/C at 0.6 V (vs. RHE) in O_2 saturated 0.1 M KOH.

calculated to be in the range from 3.85 to 3.99 over the potential range from 0.3 to 0.6 V (Fig. S15c), implying the four-electron (4e⁻) ORR pathway on single atom sites. This is because the formed metastable and coordination-unsaturated Ni-N$_x$ ($x < 4$) active sites during ORR

conditions promote the adsorption and dissociation of O_2 into *O species (a crucial intermediate of the efficient 4e⁻ pathway) [54]. In addition to the ORR activity and kinetics, long-term stability of a catalysts is another important property to be considered for its practical applications. As the

i-t response curves shown in Fig. 4f, a high current retention rate of 93.7% is achieved for Ni SAs-NC after continuously operated for 20 h, highlighting its favorable ORR stability.

3.4. Electrocatalytic UOR performance of Ni SAs-NC

The UOR electrocatalytic activity of Ni SAs-NC was then investigated in details in 1.0 M KOH and urea mixed solution. Since human urine contains 2–2.5 wt% urea (approximate 0.33 M), 0.33 M urea will be added in electrolyte as the simulated urea-rich wastewater (urine) in the evaluation of UOR performance. As depicted in Fig. 5a, a UOR potential of 1.39 V ($^{UOR}E_{j10}$) is acquired at a current density of 10 mA cm^{-2} for Ni SAs-NC. It is sharply decreased by 280 mV as compared to OER at this current density. Meanwhile, at the applied potential of 1.39 V, Ni SAs-NC exhibits a significant increased UOR current density of about 2-fold to 12-fold higher than those of Ni NPs-NC, RuO$_2$, and metal-free NC (Fig. 5b). In addition, the UOR activity ($^{UOR}E_{j10}$) of Ni SAs-NC is also comparable to those of prominent Ni-based catalysts reported recently, as summarized in Table S6.

To explore the UOR kinetics, Fig. 5c displays the corresponding Tafel slopes of the above catalysts derived from their LSV curves. In comparison with Ni NPs-NC (57 mV dec^{-1}), RuO$_2$ (62 mV dec^{-1}) and NC (261 mV dec^{-1}), Ni SAs-NC shows a smallest Tafel slope of 42 mV dec^{-1},

revealing its rapid electron transfer rate [17]. EIS measurement was then carried out to deeply explore the UOR kinetics of these catalysts, as shown in Fig. 5d and S16. It is revealed that the Ni SAs-NC has the smallest charge transfer resistance (R_{ct}), i.e., 52.7 Ω, which is consistent with its smallest Tafel slope and further demonstrates its rapid UOR kinetics. Therefore, the excellent UOR activity of Ni SAs-NC should be attributed to the rapid kinetics endowed by single atom Ni sites. In addition, the ECSA of a catalyst is proportional to its double-layer capacitance (C_{dl}), which can be measured by CV and used to evaluate the density of catalytic sites (Fig. S17). As denoted in Fig. 5e, Ni SAs-NC possesses the largest C_{dl} value (15.9 mF cm^{-2}) as compared with those of NC (4.0 mF cm^{-2}), RuO$_2$ (10.6 mF cm^{-2}) and Ni NPs-NC (13.8 mF cm^{-2}), indicating the high density of exposed single atom Ni sites of Ni SAs-NC. According to the recent findings obtained from *operando* XAS studies, the single atom Ni sites tend to attain high-valence states owing to the formation of structural distorted HOO-Ni-N$_4$ moieties under electrochemical oxidation conditions, which boost the adsorption of the reactants and intermediates on the surface of catalysts [55]. This may be the reason for the highly improved UOR activity of Ni SAs-NC. Finally, the strong electrochemical stability of Ni SAs-NC toward UOR is verified by its little changed current density after successive operation for 20 h at 1.39 V (Fig. 5f). The high current retention of Ni SAs-NC is ascribed to its well-preserved structure of highly dispersed Ni single atoms during the
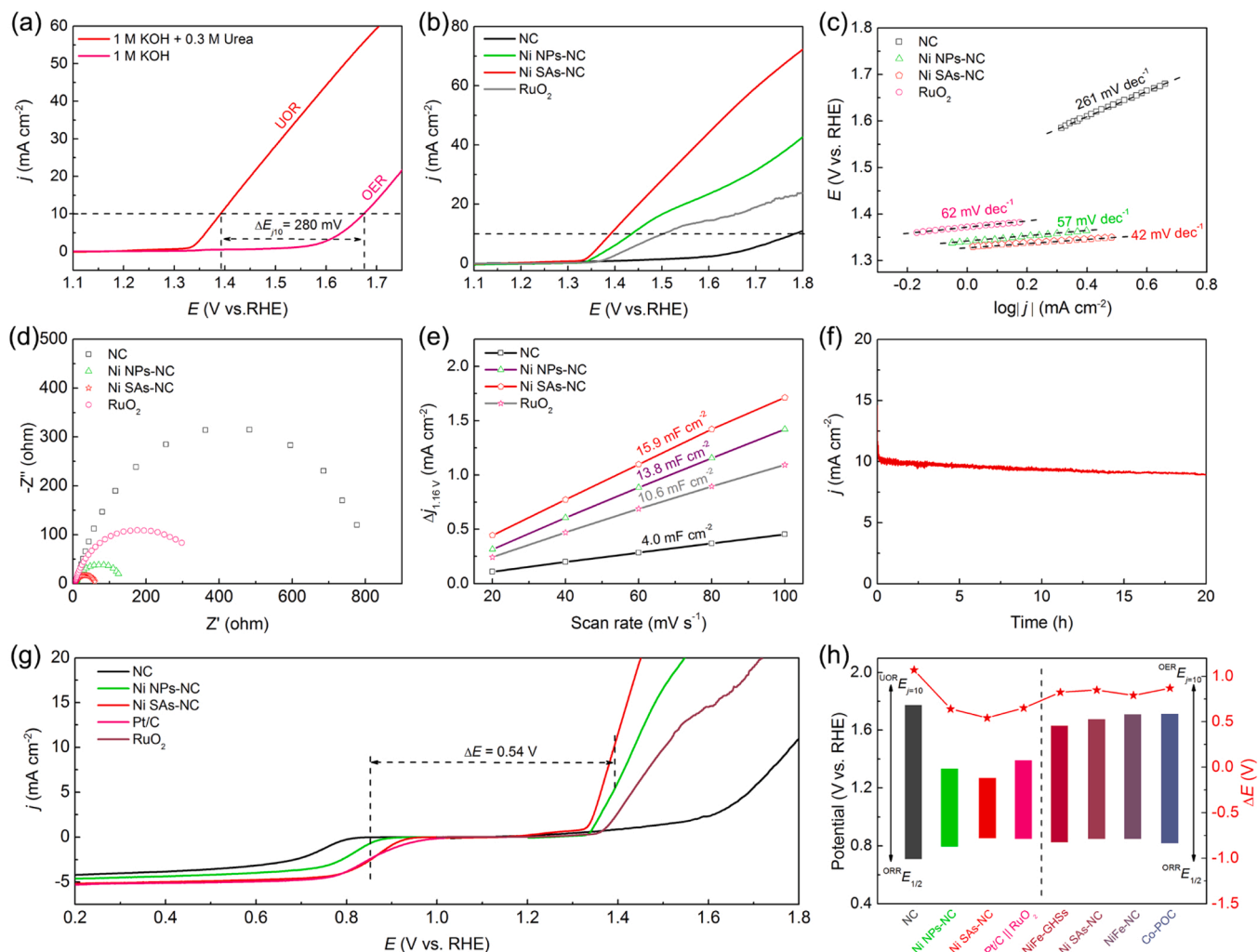

Fig. 5. (a) LSV curves of Ni SAs-NC for UOR and OER. (b) LSV curves of different catalysts for UOR in 1.0 M KOH+ 0.33 M urea. (c) The corresponding Tafel slopes, (d) Nyquist plots and (e) C_{dl} value of different catalysts. (f) The chronoamperometry response of Ni SAs-NC at 1.39 V (vs. RHE). (g) The overall polarization curves of different catalysts within the ORR and UOR potential windows. (h) Comparison of ORR/UOR and ORR/OER bifunctional electrocatalytic performance of different catalysts.

stability test, as verified by the TEM and XRD measurements (Fig. S18 and S19).

Similar to the bifunctional oxygen electrocatalysis, the potential gap (ΔE) between $^{UOR}E_{j10}$ and $^{ORR}E_{1/2}$ is defined to evaluate the overall performance of bifunctional electrocatalysts toward UOR and ORR (Eq. 4). The smaller value of ΔE is, the better is the overall performance of catalysts. As presented in Fig. 5g, Ni SAs-NC has the smallest ΔE value (0.54 V) as compared with those of Ni NPs-NC (0.64 V), Pt/C‖RuO$_2$ couple (0.65 V) and NC (1.07 V), indicating the superior bifunctional activities of Ni SAs-NC toward UOR and ORR. Remarkably, the ΔE value of Ni SAs-NC is among the smallest of almost all of bifunctional oxygen electrocatalysts reported to date (Table S7), including those based on SACs and/or dual SACs as presented in Fig. 5h, e.g., Co-POC (0.87 V) [56], NiFe-GHSs (0.79 V) [30] and NiFe-NC (0.85 V) [57]. These results demonstrate that the capability of Ni SAs-NC to be employed as a bifunctional catalyst with excellent ORR/UOR activity for urea-assisted rechargeable ZABs.

3.5. Performance of Ni SAs-NC based urea-assisted rechargeable ZAB

As a proof-of-concept study, a urea-assisted rechargeable ZAB was assembled by coupling ORR and UOR using Ni SAs-NC as bifunctional catalysts in 4 M KOH+ 0.33 M urea (Fig. S20a). For comparison, a conventional ZAB was also assembled by coupling ORR and OER using the same electrodes in 4 M KOH electrolyte (Fig. S20b). As shown in Fig. S21, a high open-circuit voltage of 1.43 V is acquired for the urea-assisted rechargeable ZAB, which is very close to that of the conventional ZAB (1.44 V). However, as disclosed by the charging/discharging polarization curves in Fig. 6a, the urea-assisted ZAB affords a lower charging voltage and an obvious reduced charging/discharging voltage gap as compared with the conventional ZAB, indicating a more efficient recharge ability of urea-assisted ZAB. Fig. 6b displays the discharging polarization (*j-V*) curves and the corresponding power density plots of the urea-assisted and conventional ZABs. The urea-assisted ZAB possesses a high peak power density of 165 mW cm^{-2}, which is extremely

close to the observed value of conventional ZAB (172 mW cm^{-2}), implying a negligible influence of urea introduction on the power density of ZABs. The insignificant influence of urea on the discharge performance of ZABs was also verified by the slightly changed mass energy density between urea-assisted and conventional ZAB (Fig. S22).

Fig. 6c shows the galvanostatic charging curves of batteries at the high current densities from 20 to 100 mA cm^{-2}. Apparently, the urea-assisted ZAB exhibits lower charging voltages at different current densities than those of conventional ZAB, leading to about 7–12% energy conservation in the charging process. These results demonstrate that coupling UOR and ORR in cathode is favorable for decreasing the charging voltage of rechargeable ZABs, and thus improving its energy conversion efficiency. In addition, the urea elimination of simulated urea-rich wastewater (urine) can also be achieved through the anodic UOR during the charging process of urea-assisted ZAB. Specifically, the urea elimination rates from 12.7 to 68.8 g m^{-2} h^{-1} (with the faradaic efficiency from 96.4% to 87.9%) are obtained over the current densities range from 20 to 100 mA cm^{-2} (Fig. 6d). Predictably, the urea elimination rate of urea-assisted ZAB will perform better under a larger current density. It should be mentioned, however, that the corresponding faradaic efficiency of UOR will also drop rapidly owing to the existence of competing OER at a high voltage. Finally, to evaluate the energy conversion efficiency and cyclic stability of Ni SAs-NC based urea-assisted ZABs, galvanostatic charging/discharging measurements were carried out at 10 mA cm^{-2}. As presented in Fig. 6e, the urea-assisted ZAB exhibits a small charging/discharging voltage gap (0.48 V) and a high energy conversion efficiency (71.8%), surpassing the Ni SAs-NC based conventional rechargeable ZAB (0.77 V, 61.3%) and the great majority of reported conventional rechargeable ZABs (Table S8). These results coincide with the analysis of charging/discharging polarization curves, indicating the superior UOR/ORR bifunctional activities of Ni SAs-NC and the better charging ability of urea-assisted ZAB due to its more favorable cathodic UOR. Remarkably, the voltage gap remains almost unchanged even after operation for 300 cycles (a total of 300 h) for both urea-assisted ZAB and conventional
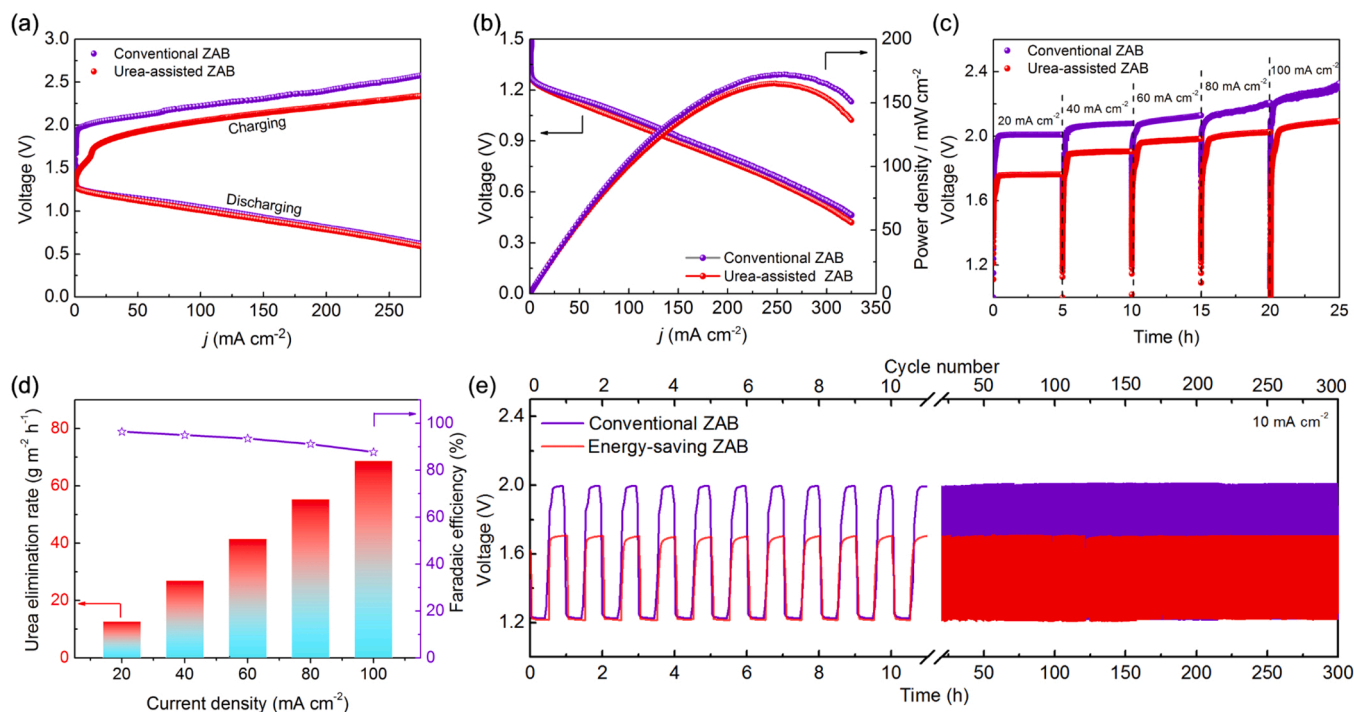

Fig. 6. (a) Charging/discharging polarization (*j-V*) curves, (b) discharging polarization (*j-V*) curves and the corresponding power density plots of urea-assisted and conventional ZABs. (c) Galvanostatic charging curves of urea-assisted and conventional ZABs at different current densities. (d) Urea elimination rates and the corresponding faradaic efficiencies for the Ni SAs-NC based urea-assisted ZAB at different current densities. (e) Galvanostatic charging/discharging cycling curves of the urea-assisted and conventional ZABs at 10 mA cm^{-2}.

ZAB (Fig. S23), demonstrating an outstanding stability of Ni SAs-NC catalyst toward both UOR and ORR in practical batteries.

4. Conclusions

In summary, we have successfully synthesized a bifunctional ORR/UOR electrocatalyst comprising Ni single atoms anchored on N-doped carbon nanosheets (Ni SAs-NC), and based on it developed a conceptual urea-assisted rechargeable ZAB. Due to the individually dispersed and highly exposed Ni-N$_4$ sites, the as-obtained Ni SAs-NC catalyst was endowed with remarkable ORR/UOR bifunctional electrocatalytic activities and strong durability in alkaline electrolyte. Specifically, it exhibits a small potential gap ($\Delta E = 0.54$ V) between the potential at 10 mA/cm^{-2} for UOR ($^{UOR}E_{j10}$) and the half-wave potential for ORR ($^{ORR}E_{1/2}$). The as-assembled urea-assisted rechargeable ZABs using Ni SAs-NC as electrocatalysts keep an excellent discharging ability and deliver a significantly decreased charging voltage, thus acquiring a high energy conversion efficiency of 71.8% (improved by 17.1% as compares with the conventional ZABs coupling ORR and OER). Additionally, a urea elimination rate of 68.8 gm^{-2}h^{-1} (with a faradaic efficiency of 87.9%) is achieved at the cathode chamber under a charging current density of 100 mA cm^{-2}. This work not only opens up a new application field for Ni SACs, but also provides potential opportunities for developing a novel electrochemical energy storage device with high energy conversion efficiency.

CRediT authorship contribution statement

Hao Jiang: Conceptualization, Investigation, Data curation, Writing – original draft. **Jing Xia:** Investigation, Data curation. **Long Jiao:** Data curation. **Xiangmin Meng:** Conceptualization. **Pengfei Wang:** Validation. **Chun-Sing Lee:** Formal analysis. **Wenjun Zhang:** Writing – review & editing, Validation, Supervision.

Declaration of Competing Interest

The authors declare that they have no known competing financial interests or personal relationships that could have appeared to influence the work reported in this paper.

Acknowledgements

Appendix A. Supporting information

Supplementary data associated with this article can be found in the online version at doi:10.1016/j.apcatb.2022.121352.

References

[1] M. Liu, P. Zhang, Z. Qu, Y. Yan, C. Lai, T. Liu, S. Zhang, Conductive carbon nanofiber interpenetrated graphene architecture for ultra-stable sodium ion battery, Nat. Commun. 10 (2019) 1–11, https://doi.org/10.1038/s41467-019-11925-z.

[2] Y. Yan, P. Zhang, Z. Qu, M. Tong, S. Zhao, Z. Li, M. Liu, Z. Lin, Carbon/sulfur aerogel with adequate mesoporous channels as robust polysulfide confinement matrix for highly stable lithium-sulfur battery, Nano Lett. 20 (2020) 7662–7669, https://doi.org/10.1021/acs.nanolett.0c03203.

[3] L. Zhou, S.Y. Lu, S. Guo, Recent progress on precious metal single atom materials for water splitting catalysis, SusMat 1 (2021) 194–210, https://doi.org/10.1002/sus2.15.

[4] X. Yuan, F. Ma, L. Zuo, J. Wang, N. Yu, Y. Chen, Y. Zhu, Q. Huang, R. Holze, Y. Wu, Latest advances in high-voltage and high-energy-density aqueous rechargeable batteries, Electrochem. Energy Rev. 4 (2021) 1–34, https://doi.org/10.1007/s41918-020-00075-2.

[5] Y. Li, H. Dai, Recent advances in zinc-air batteries, Chem. Soc. Rev. 43 (2014) 5257–5275.

[6] T. Zhou, N. Zhang, C. Wu, Y. Xie, Surface/interface nanoengineering for rechargeable Zn-air batteries, Energy Environ. Sci. 13 (2020) 1132–1153, https://doi.org/10.1039/C9EE03634B.

[7] Y. Wang, K. Wang, J. Yu, Y. Ma, X. Yang, H. Jiang, Y. Liu, J. Li, W. Li, 3D spiral-like polyhedron nanocarbon confining uniformly dispersed Co nanoparticles for bifunctional electrocatalyst in metal-air battery, J. Power Sources 482 (2021), 228897, https://doi.org/10.1016/j.jpowsour.2020.228897.

[8] S. Zhang, M. Chen, X. Zhao, J. Cai, W. Yan, J.C. Yen, S. Chen, Y. Yu, J. Zhang, Advanced noncarbon materials as catalyst supports and non-noble electrocatalysts for fuel cells and metal-air batteries, Electrochem. Energy Rev. 4 (2021) 336–381, https://doi.org/10.1007/s41918-020-00085-0.

[9] H. Jiang, C. Li, H. Shen, Y. Liu, W. Li, J. Li, Supramolecular gel-assisted synthesis Co$_2$P particles anchored in multielement co-doped graphene as efficient bifunctional electrocatalysts for oxygen reduction and evolution, Electrochim. Acta 231 (2017) 344–353, https://doi.org/10.1016/j.electacta.2017.02.074.

[10] X. Cui, L. Gao, S. Lei, S. Liang, J. Zhang, C.D. Sewell, W. Xue, Q. Liu, Z. Lin, Y. Yang, Simultaneously crafting single-atomic Fe sites and graphitic layer-wrapped Fe$_3$C nanoparticles encapsulated within mesoporous carbon tubes for oxygen reduction, Adv. Funct. Mater. 31 (2021), 2009197, https://doi.org/10.1002/adfm.202009197.

[11] F. Dong, M. Wu, Z. Chen, X. Liu, G. Zhang, J. Qiao, S. Sun, Atomically dispersed transition metal-nitrogen-carbon bifunctional oxygen electrocatalysts for zinc-air batteries: recent advances and future perspectives, Nano Micro Lett. 14 (2022) 1–25, https://doi.org/10.1007/s40820-021-00768-3.

[12] Y. Yan, S. Liang, X. Wang, M. Zhang, S.-M. Hao, X. Cui, Z. Li, Z. Lin, Robust wrinkled MoS$_2$/NC bifunctional electrocatalysts interfaced with single Fe atoms for wearable zinc-air batteries, Proc. Natl. Acad. Sci. U.S.A. 118 (2021), e2110036118, https://doi.org/10.1073/pnas.2110036118.

[13] A. Wang, C. Zhao, M. Yu, W. Wang, Trifunctional Co nanoparticle confined in defect-rich nitrogen-doped graphene for rechargeable Zn-air battery with a long lifetime, Appl. Catal. B 281 (2021), 119514, https://doi.org/10.1016/j.apcatb.2020.119514.

[14] Y. Meng, J.-C. Li, S.-Y. Zhao, C. Shi, X.-Q. Li, L. Zhang, P.-X. Hou, C. Liu, H.-M. Cheng, Fluorination-assisted preparation of self-supporting single-atom Fe-N-doped single-wall carbon nanotube film as bifunctional oxygen electrode for rechargeable Zn-Air batteries, Appl. Catal. B 294 (2021), 120239, https://doi.org/10.1016/j.apcatb.2021.120239.

[15] Z. Zhu, Q. Xu, Z. Ni, K. Luo, Y. Liu, D. Yuan, CoNi nanoalloys@N-doped graphene encapsulated in N-doped carbon nanotubes for rechargeable Zn-air batteries, ACS Sustain. Chem. Eng. 9 (2021) 13491–13500, https://doi.org/10.1021/acssuschemeng.1c04259.

[16] B. Zhu, Z. Liang, R. Zou, Designing advanced catalysts for energy conversion based on urea oxidation reaction, Small 16 (2020), 1906133, https://doi.org/10.1002/smll.201906133.

[17] H. Jiang, M. Sun, S. Wu, B. Huang, C.S. Lee, W. Zhang, Oxygen-incorporated NiMoP nanotube arrays as efficient bifunctional electrocatalysts for urea-assisted energy-saving hydrogen production in alkaline electrolyte, Adv. Funct. Mater. (2021), 2104951, https://doi.org/10.1002/adfm.202104951.

[18] Q. Zhang, F.M. Kazim, S. Ma, K. Qu, M. Li, Y. Wang, H. Hu, W. Cai, Z. Yang, Nitrogen dopants in nickel nanoparticles embedded carbon nanotubes promote overall urea oxidation, Appl. Catal. B 280 (2021) 119436, https://doi.org/10.1016/j.apcatb.2020.119436.

[19] H. Zhang, X. Meng, J. Zhang, Y. Huang, Hierarchical NiFe hydroxide/Ni$_3$N nanosheet-on-nanosheet heterostructures for bifunctional oxygen evolution and urea oxidation reactions, ACS Sustain. Chem. Eng. 9 (2021) 12584–12590, https://doi.org/10.1021/acssuschemeng.1c03353.

[20] S. Yi, H. Jiang, X. Bao, S. Zou, J. Liao, Z. Zhang, Recent progress of Pt-based catalysts for oxygen reduction reaction in preparation strategies and catalytic mechanism, J. Electroanal. Chem. 848 (2019), 113279, https://doi.org/10.1016/j.jelechem.2019.113279.

[21] X. Zhong, S. Ye, J. Tang, Y. Zhu, D. Wu, M. Gu, H. Pan, B. Xu, Engineering Pt and Fe dual-metal single atoms anchored on nitrogen-doped carbon with high activity and durability towards oxygen reduction reaction for zinc-air battery, Appl. Catal. B 286 (2021), 119891, https://doi.org/10.1016/j.apcatb.2021.119891.

[22] M. Li, F. Tian, T. Lin, L. Tao, X. Guo, Y. Chao, Z. Guo, Q. Zhang, L. Gu, W. Yang, High-index faceted PdPtCu ultrathin nanorings enable highly active and stable oxygen reduction electrocatalysis, Small Methods (2021), 2100154, https://doi.org/10.1002/smtd.202100154.

[23] V. Vij, S. Sultan, A.M. Harzandi, A. Meena, J.N. Tiwari, W. Lee, T. Yoon, K.S. Kim, Nickel-based electrocatalysts for energy-related applications: oxygen reduction, oxygen evolution, and hydrogen evolution reactions, ACS Catal. 7 (2017) 7196–7225, https://doi.org/10.1021/acscatal.7b01800.

[24] Q. Lu, X. Zou, C. Wang, K. Liao, P. Tan, R. Ran, W. Zhou, M. Ni, Z. Shao, Tailoring charge and mass transport in cation/anion-codoped Ni$_3$N/N-doped CNT integrated electrode toward rapid oxygen evolution for fast-charging zinc-air batteries, Energy Stor. Mater. 39 (2021) 11–20, https://doi.org/10.1016/j.ensm.2021.04.013.

[25] J. Balamurugan, T.T. Nguyen, D.H. Kim, N.H. Kim, J.H. Lee, 3D nickel molybdenum oxyselenide (Ni$_{1-x}$Mo$_x$OSe) nanoarchitectures as advanced multifunctional catalyst for Zn-air batteries and water splitting, Appl. Catal. B 286 (2021), 119909, https://doi.org/10.1016/j.apcatb.2021.119909.

[26] L. Lei, D. Huang, M. Cheng, R. Deng, S. Chen, Y. Chen, W. Wang, Defects engineering of bimetallic Ni-based catalysts for electrochemical energy conversion, Coord. Chem. Rev. 418 (2020), 213372, https://doi.org/10.1016/j.ccr.2020.213372.

[27] C. Lai, J. Fang, X. Liu, M. Gong, T. Zhao, T. Shen, K. Wang, K. Jiang, D. Wang, In situ coupling of NiFe nanoparticles with N-doped carbon nanofibers for Zn-air batteries driven water splitting, Appl. Catal. B 285 (2021), 119856, https://doi.org/10.1016/j.apcatb.2020.119856.

[28] Q. Zhang, J. Guan, Single-atom catalysts for electrocatalytic applications, Adv. Funct. Mater. 30 (2020), 2000768, https://doi.org/10.1002/adfm.202000768.

[29] X. Zhang, S. Zhang, Y. Yang, L. Wang, Z. Mu, H. Zhu, X. Zhu, H. Xing, H. Xia, B. Huang, A general method for transition metal single atoms anchored on honeycomb-like nitrogen-doped carbon nanosheets, Adv. Mater. 32 (2020), 1906905, https://doi.org/10.1002/adma.201906905.

[30] J. Chen, H. Li, C. Fan, Q. Meng, Y. Tang, X. Qiu, G. Fu, T. Ma, Dual single-atomic Ni-N₄ and Fe-N₄ sites constructing janus hollow graphene for selective oxygen electrocatalysis, Adv. Mater. 32 (2020), 2003134, https://doi.org/10.1002/adma.202003134.

[31] H.J. Qiu, P. Du, K. Hu, J. Gao, H. Li, P. Liu, T. Ina, K. Ohara, Y. Ito, M. Chen, Metal and nonmetal codoped 3D nanoporous graphene for efficient bifunctional electrocatalysis and rechargeable Zn-air batteries, Adv. Mater. 31 (2019), 1900843, https://doi.org/10.1002/adma.201900843.

[32] Z. Yu, C. Lang, M. Gao, Y. Chen, Q. Fu, Y. Duan, S. Yu, Ni-Mo-O nanorod-derived composite catalysts for efficient alkaline water-to-hydrogen conversion via urea electrolysis, Energy Environ. Sci. 11 (2018) 1890–1897, https://doi.org/10.1039/c8ee00521d.

[33] L. Zhang, L. Wang, H. Lin, Y. Liu, J. Ye, Y. Wen, A. Chen, L. Wang, F. Ni, Z. Zhou, A lattice-oxygen-involved reaction pathway to boost urea oxidation, Angew. Chem. Int. Ed. 58 (2019) 16820–16825, https://doi.org/10.1002/ange.201909832.

[34] T. With, T.D. Petersen, B. Petersen, A simple spectrophotometric method for the determination of urea in blood and urine, J. Clin. Pathol. 14 (1961) 202–204, https://doi.org/10.1136/jcp.14.2.202.

[35] G. Chen, P. Liu, Z. Liao, F. Sun, Y. He, H. Zhong, T. Zhang, E. Zschech, M. Chen, G. Wu, Zinc-mediated template synthesis of Fe-N-C electrocatalysts with densely accessible Fe-Nₓ active sites for efficient oxygen reduction, Adv. Mater. 32 (2020), 1907399, https://doi.org/10.1002/adma.201907399.

[36] H. Jiang, Y.Q. Wang, J.Y. Hao, Y.S. Liu, W.Z. Li, J. Li, N and P co-functionalized three-dimensional porous carbon networks as efficient metal-free electrocatalysts for oxygen reduction reaction, Carbon 122 (2017) 64–73, https://doi.org/10.1016/j.carbon.2017.06.043.

[37] P. Wang, R. Qin, P. Ji, Z. Pu, J. Zhu, C. Lin, Y. Zhao, H. Tang, W. Li, S. Mu, Synergistic coupling of Ni nanoparticles with Ni₃C nanosheets for highly efficient overall water splitting, Small 16 (2020), 2001642, https://doi.org/10.1002/smll.202001642.

[38] N.K. Wagh, S.S. Shinde, C.H. Lee, J. Jung, D. Kim, S. Kim, C. Lin, S.U. Lee, J. Lee, Densely colonized isolated Cu-N single sites for efficient bifunctional electrocatalysts and rechargeable advanced Zn-air batteries, Appl. Catal. B 268 (2020), 118746, https://doi.org/10.1016/j.apcatb.2020.118746.

[39] K. Mou, Z. Chen, X. Zhang, M. Jiao, X. Zhang, X. Ge, W. Zhang, L. Liu, Highly efficient electroreduction of CO₂ on nickel single-atom catalysts: atom trapping and nitrogen anchoring, Small 15 (2019), 1903668 https://doi.org/0.1002/smll.201903668.

[40] K. Jiang, S. Siahrostami, T. Zheng, Y. Hu, S. Hwang, E. Stavitski, Y. Peng, J. Dynes, M. Gangisetty, D. Su, Isolated Ni single atoms in graphene nanosheets for high-performance CO₂ reduction, Energy Environ. Sci. 11 (2018) 893–903, https://doi.org/10.1039/C7EE03245E.

[41] H.B. Yang, S. Hung, S. Liu, K. Yuan, S. Miao, L. Zhang, X. Huang, H. Wang, W. Cai, R. Chen, Atomically dispersed Ni (I) as the active site for electrochemical CO₂ reduction, Nat. Energy 3 (2018) 140–147, https://doi.org/10.1038/s41560-017-0078-8.

[42] J. Yu, Y. Wang, L. Zhu, H. Jiang, J. Hao, Y. Zhang, M. Liu, J. Li, X. Ji, W. Li, Chirality induces the self-assembly to generate a 3D porous spiral-like polyhedron as metal-free electrocatalysts for the oxygen reduction reaction, ACS Appl. Mater. Interfaces 11 (2019) 45596–45605, https://doi.org/10.1021/acsami.9b14775.

[43] L. Bai, C. Hsu, D.T. Alexander, H.M. Chen, X. Hu, A cobalt-iron double-atom catalyst for the oxygen evolution reaction, J. Am. Chem. Soc. 141 (2019) 14190–14199, https://doi.org/10.1021/jacs.9b05268.

[44] W. Liu, Y. Chen, H. Qi, L. Zhang, W. Yan, X. Liu, X. Yang, S. Miao, W. Wang, C. Liu, A durable nickel single-atom catalyst for hydrogenation reactions and cellulose valorization under harsh conditions, Angew. Chem. Int. Ed. 130 (2018) 7189–7193, https://doi.org/10.1002/ange.201802231.

[45] A. Zitolo, V. Goellner, V. Armel, M.-T. Sougrati, T. Mineva, L. Stievano, E. Fonda, F. Jaouen, Identification of catalytic sites for oxygen reduction in iron-and nitrogen-doped graphene materials, Nat. Mater. 14 (2015) 937–942, https://doi.org/10.1038/nmat4367.

[46] Q. He, D. Liu, J.H. Lee, Y. Liu, Z. Xie, S. Hwang, S. Kattel, L. Song, J.G. Chen, Electrochemical conversion of CO₂ to syngas with controllable CO/H₂ ratios over Co and Ni single-atom catalysts, Angew. Chem. Int. Ed. 59 (2020) 3033–3037, https://doi.org/10.1002/anie.201912719.

[47] S.-G. Han, D.-D. Ma, S.-H. Zhou, K. Zhang, W.-B. Wei, Y. Du, X.-T. Wu, Q. Xu, R. Zou, Q.-L. Zhu, Fluorine-tuned single-atom catalysts with dense surface Ni-N₄ sites on ultrathin carbon nanosheets for efficient CO₂ electroreduction, Appl. Catal. B 283 (2021), 119591, https://doi.org/10.1016/j.apcatb.2020.119591.

[48] Y. Zhou, X. Tao, G. Chen, R. Lu, D. Wang, M.-X. Chen, E. Jin, J. Yang, H.-W. Liang, Y. Zhao, Multilayer stabilization for fabricating high-loading single-atom catalysts, Nat. Commun. 11 (2020) 1–11, https://doi.org/10.1038/s41467-020-19599-8.

[49] Z. Zhang, X. Zhao, S. Xi, L. Zhang, Z. Chen, Z. Zeng, M. Huang, H. Yang, B. Liu, S. J. Pennycook, Atomically dispersed cobalt trifunctional electrocatalysts with tailored coordination environment for flexible rechargeable Zn-air battery and self-driven water splitting, Adv. Energy Mater. 10 (2020), 2070195, https://doi.org/10.1002/aenm.202002896.

[50] P. Du, K. Hu, J. Lyu, H. Li, X. Lin, G. Xie, X. Liu, Y. Ito, H. Qiu, Anchoring Mo single atoms/clusters and N on edge-rich nanoporous holey graphene as bifunctional air electrode in Zn-air batteries, Appl. Catal. B 276 (2020), 119172, https://doi.org/10.1016/j.apcatb.2020.119172.

[51] X. Zhu, R. Amal, X. Lu, N, P Co-coordinated manganese atoms in mesoporous carbon for electrochemical oxygen reduction, Small 15 (2019), 1804524, https://doi.org/10.1002/smll.201804524.

[52] H. Jiang, J.X. Gu, X.S. Zheng, M. Liu, X.Q. Qiu, L.B. Wang, W.Z. Li, Z.F. Chen, X. B. Ji, J. Li, Defect-rich and ultrathin N doped carbon nanosheets as advanced trifunctional metal-free electrocatalysts for the ORR, OER and HER, Energy Environ. Sci. 12 (2019) 322–333, https://doi.org/10.1039/C8EE03276A.

[53] H. Jiang, Y. Liu, W. Li, J. Li, Co nanoparticles confined in 3D nitrogen-doped porous carbon foams as bifunctional electrocatalysts for long-life rechargeable Zn-air batteries, Small 14 (2018), 1703739, https://doi.org/10.1002/smll.201703739.

[54] H. Su, W. Zhou, H. Zhang, W. Zhou, X. Zhao, Y. Li, M. Liu, W. Cheng, Q. Liu, Dynamic evolution of solid-liquid electrochemical interfaces over single-atom active sites, J. Am. Chem. Soc. 142 (2020) 12306–12313, https://doi.org/10.1021/jacs.0c04231.

[55] W. Wan, C.A. Triana, J. Lan, J. Li, C.S. Allen, Y. Zhao, M. Iannuzzi, G.R. Patzke, Bifunctional single atom electrocatalysts: coordination-performance correlations and reaction pathways, ACS Nano 14 (2020) 13279–13293, https://doi.org/10.1021/acsnano.0c05088.

[56] B.Q. Li, C.X. Zhao, S. Chen, J.N. Liu, X. Chen, L. Song, Q. Zhang, Framework-porphyrin-derived single-atom bifunctional oxygen electrocatalysts and their applications in Zn-air batteries, Adv. Mater. 31 (2019), 1900592, https://doi.org/10.1002/adma.201900592.

[57] M. Ma, A. Kumar, D. Wang, Y. Wang, Y. Jia, Y. Zhang, G. Zhang, Z. Yan, X. Sun, Boosting the bifunctional oxygen electrocatalytic performance of atomically dispersed Fe site via atomic Ni neighboring, Appl. Catal. B 274 (2020), 119091, https://doi.org/10.1016/j.apcatb.2020.119091.